Genetic Algorithm-based Control of a Modular On-Board Charger for Electric Vehicle Applications

Fatemeh Nasr Esfahani
School of Engineering
Lancaster University
Lancaster, UK
f.nasresfahani@lancaster.ac.uk

Mohammadreza Parvizimosaed
Smith Engineering
Queen's University
Kingston, Canada
m.parvizimosaed@queensu.ca

Javad Ebrahimi
Smith Engineering
Queen's University
Kingston, Canada
javad.ebrahimi@queensu.ca

Alireza Bakhshai
Smith Engineering
Queen's University
Kingston, Canada
alireza.bakhshai@queensu.ca

Xiandong Ma
School of Engineering
Lancaster University
Lancaster, UK
xiandong.ma@lancaster.ac.uk

Ahmed Darwish
School of Engineering
Lancaster University
Lancaster, UK
a.badawy@lancaster.ac.uk

***Index Terms*—≪Electric Vehicle (EV)≫, ≪Genetic Algorithm≫, ≪Integrated On-board Charger≫, ≪Modular Converter≫, ≪PR-Controller≫**

***Abstract*—This paper presents the operation and control of a modular on-board charger (OBC) for electric vehicle (EV) applications. The modular design enhances fault tolerance, scalability, and thermal management, making it suitable for high-power EV applications. Single-stage isolated Cuk-based converters are used as submodules, supporting bidirectional power flow for enhanced energy efficiency. Additionally, the modular OBC operates efficiently in various modes, including normal driving, regenerative braking, and grid-connected charging, thanks to its integrated structure. A key innovation is the implementation of genetic algorithm (GA)-based controllers, which optimise control parameters to address the right-half-plane (RHP) zero challenges inherent in Cuk converters, thereby improving system stability and dynamic performance. Simulation and experimental results in charging mode demonstrate robust performance, highlighting precise grid current control, effective power factor correction, and stable battery charging under both normal and partial fault conditions.**

I. Introduction

The transport sector significantly contributes to greenhouse gas (GHG) emissions, with internal combustion engines (ICEs) accounting for 29% of GHG emissions. To mitigate these impacts, there is a global shift towards electric vehicles (EVs) [1]–[3].

EVs' essential components include electric motors, high-voltage (HV) battery packs, low-voltage (LV) systems, and traction converters [4], [5]. Charging infrastructure includes both on-board chargers (OBCs) and off-board chargers. While off-board chargers support fast charging, they face limitations due to installation costs and location constraints [6], [7]. Integrated into EVs, OBCs offer flexibility for standard charging locations [8]–[11].

Many EVs use series-connected HV battery packs to extend range, but this setup poses challenges such as reduced efficiency from increased resistance, accelerated degradation, and safety risks from voltage imbalances and heat [12]. Modularising HV battery systems addresses these issues by dividing the battery into smaller modules. This modular approach enhances safety, reduces stress on semiconductor devices, improves efficiency, and provides greater flexibility for upgrades and replacements [13], [14]. Additionally, it improves battery monitoring, fault detection, and fault ride-through capabilities [15], [16].

Several studies have explored modular topologies, where the output stages of power modules can be interconnected to enhance overall power capacity [17], [18]. Dual active bridge (DAB) configurations are prevalent in galvanically isolated modular converters used for EV applications [19], [20]. While modularised battery chargers were developed in the literature to enable paralleling of power converters and increase power density, there has been a lack of discussion regarding modularising the HV battery system.

This paper introduces a novel modular power converter designed for EVs. This system is bidirectional and supports various operational modes: (i) normal driving mode, where power flows from the batteries to the motor, (ii) regenerative braking mode, where power is reversed to recharge the batteries, and (iii) charging mode, where power is drawn from the AC grid to charge the batteries

[21], [22]. While various converter structures could be utilised as the submodule (SM) in the OBC charger's power stage, this paper focuses on the single-stage Cuk inverter. The Cuk topology offers the advantage of providing a flexible output voltage that can be either above or below the input battery voltage. It supports the use of a high-frequency transformer to ensure galvanic isolation between the input and output sides. This isolation not only enables additional voltage boosting but also meets safety standards specified in IEC 60950, which is crucial when the EV is in charging mode [23]. Furthermore, the Cuk converter's continuous input and output currents necessitate only small capacitors at both the battery and output sides.

The Cuk converter's transfer function includes right-half-plane (RHP) zeros, which can introduce challenges such as system instability and degraded transient response. To address these issues, genetic algorithm (GA)-based controllers are used to design the controller gains. The GA-based approach allows for effective optimisation of the controller parameters, accommodating the unique characteristics and constraints imposed by the RHP zeros in the Cuk converter's transfer function.

The rest of this paper is organised as follows: Section II details the modular OBC's design. Section III covers the operational modes of the Cuk-based SMs, including rectification and inversion. Sections IV and V describe the controller design and the use of the GA, respectively. Simulations and experimental results for the charging mode are presented in Section VI. The paper concludes in Section VII.

II. System Description

Fig. 1 illustrates the overall configuration of the modular OBC designed for EV applications. The modular architecture enhances scalability, fault tolerance, and thermal management, making it suitable for high-power EV systems. In this design, each battery segment is connected to three SMs, with one SM assigned to each phase (phases a, b, and c). The SMs within each phase are connected in series to form the three-phase output voltages and currents. The output of the m cascaded SMs in each phase is connected to the AC terminal, which can interface with either the AC grid or the vehicle's motor.

The HV battery is modularised into multiple segments, each supplying a specific number of SMs. Each battery segment consists of p series-connected battery packs, and each battery pack contains c parallel battery cells. The total number of HV battery packs n and the total number of parallel battery cells n_t can be determined as follows:

$$\begin{cases} n = p \times m \\ n_{\mathrm{t}} = n \times c \end{cases} . \tag{1}$$

The number of SMs (m) per phase depends on the desired output voltage and power level. Typically, for high-power EV applications, m ranges from 3 to 6 SMs per phase. This allows flexibility in scaling the system to meet different voltage and power requirements.

A Cuk-based converter serves as the SM for this charger, which is capable of working as both a DC-to-AC inverter (in driving and V2G modes) and an AC-to-DC rectifier (in regenerative braking and charging modes).

The system employs three single-phase single-pole double-throw switches SW_j (where $j = a, b, c$), to switch between these operational modes, connecting the SMs in each phase to either the AC grid or the permanent magnet synchronous machine (PMSM).

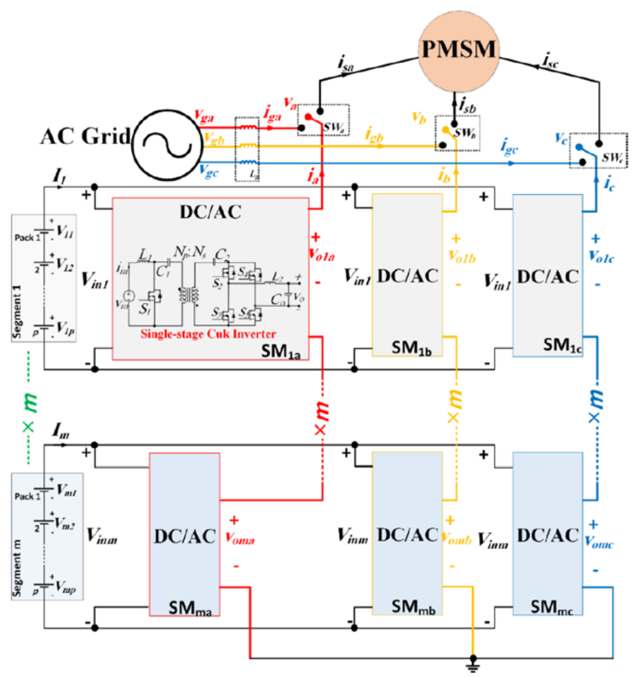

Fig. 1 : Three-phase configuration of the modular OBC

The SMs within each phase are connected in series, collectively forming the three-phase currents i_j and voltages v_j, where j represents phases a, b, and c. The output three-phase currents and voltages of the modular topology are determined as follows:

$$i_j(t) = I_o \sin\left(\omega t + \varphi_j + \gamma\right), \tag{2}$$

$$v_j(t) = \sum_{k=1}^{m} v_{o_{k_j}}(t) = V_o \sin\left(\omega t + \varphi_j + \delta\right), \tag{3}$$

where $\varphi_j = \{0, -\frac{2\pi}{3}, \frac{2\pi}{3}\}$ and $k = 1 : m$. Also, $v_{o_{k_j}}$ is the output voltage of the k^{th} SM in phase "j".

The output current of the k^{th} battery segment can be approximated by $I_k \approx \dfrac{3V_o I_o \cos(\delta - \gamma)}{2mV_{in_k}\eta_{SM}}$, where η_{SM} represents the efficiency of the Ćuk-based SMs. Here, $V_{in_k} = \sum_{i=1}^{p} V_{k_i}$ represents the total voltage of the k^{th} battery segment.

The modular design allows flexibility in configuring the voltage levels. For instance, if each battery pack provides 48 V and four packs are connected in series per segment ($p = 4$), the segment voltage would be approximately 192 V. With three segments ($m = 3$) per phase, the total DC-link voltage per phase would be around 576 V. This voltage can be adjusted by varying the number of SMs and battery packs per segment to meet specific EV requirements.

III. Modes of Operation

This section details the operational principles of the Cuk-based SM across various modes. It includes extracting the transfer function used in the controller design.

A. Inverter Operation

In the DC-to-AC inverter mode, the SM converts the constant DC power from the batteries into variable voltage and frequency AC power, suitable for driving the PMSM.

Fig. 2 illustrates the switching operation of the Cuk-based SM inverter during the positive half-cycle of the output voltage v_o. The parameters governing the switching and activation times are t_s and t_{ON}, respectively. In Fig. 2a, switches S_1, S_2, and S_5 are in the ON-state within the time interval $0 \leq t < t_{ON}$, causing a drop in the capacitor voltages v_{C_1} and v_{C_2}, while the input current i_{in} and output current i_o rise.

In Fig. 2b, during the time interval $t_{ON} \leq t < t_s$, all switches except S_5 are in the OFF-state. This results in a decrease in both i_{in} and i_o, with v_{C_1} and v_{C_2} increasing. The main waveforms of the SM during these states are shown in Fig. 2c, with $N = N_s/N_p$ representing the turns ratio of the high-frequency transformer.

During the negative half-cycle of v_o, switches S_3 and S_4 are in the ON-state, replacing S_2 and S_5 to charge the inductors L_1 and L_2. In the second interval, all switches except S_3 are in the OFF-state, discharging L_1 and L_2 into C_1 and C_2, as well as the output capacitor C_o.

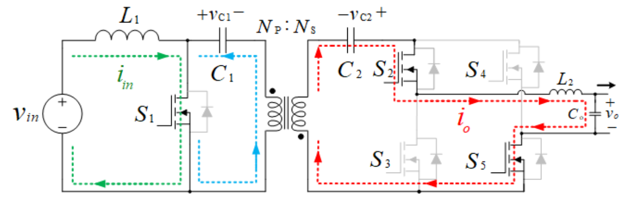

(a) ON-state (t_{ON})

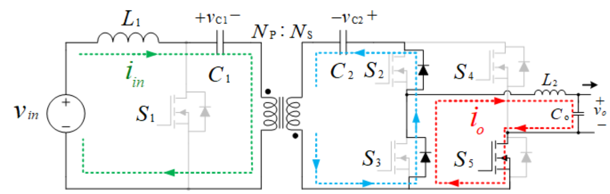

(b) OFF-state ($t_{OFF} = t_s - t_{ON}$)

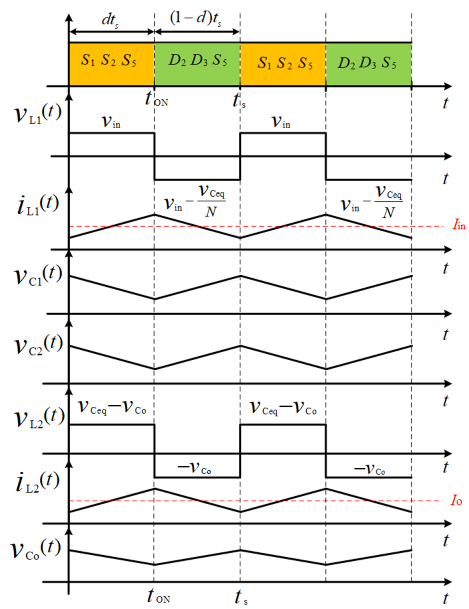

(c) Key waveforms for the positive half-cycle

Fig. 2 : Inverter operation of the Cuk-based SM in the positive half-cycle $v_o > 0$

B. Rectifier Operation

Fig. 3 illustrates the rectifier operation of the Cuk-based SM, showing its role in charging battery packs from the AC grid or the PMSM when acting as a permanent magnet synchronous generator (PMSG). During regenerative braking, the SM functions as an AC-to-DC rectifier, capturing the kinetic energy from braking and converting it into DC power for the batteries. Similarly, in charging mode, the SM also serves as an AC-to-DC rectifier, transforming AC power from the main supply into DC power suitable for battery charging.

In Fig. 3, the input and output currents i_{in} and i_o reverse direction when the Cuk-based SM operates as a rectifier. Fig. 3a shows that during $0 \leq t < t_{\mathrm{ON}}$ with a positive v_o, switches S_2 and S_3 are in the ON-state. Consequently, capacitors C_1 and C_2 discharge into inductor L_1, increasing i_{in}. Simultaneously, inductor L_2 is charged by the output capacitor C_o, raising i_o. During the interval $t_{\mathrm{ON}} \leq t < t_s$, as shown in Fig. 3b, all switches are in the OFF-state, leading to a decrease in i_{in} and i_o, while v_{C_1} and v_{C_2} increase. The primary waveforms of the SM during these phases are shown in Fig. 3c.

For the negative half-cycle of v_o, switches S_4 and S_5 are in the ON-state, replacing S_2 and S_3 during $0 \leq t < t_{\mathrm{ON}}$. In the subsequent interval $t_{\mathrm{ON}} \leq t < t_s$, the current flows through diodes D_3 and D_4 on the secondary side, from L_2 to capacitors C_1 and C_2.

The voltages across the two capacitors C_1 and C_2 change in tandem. Consequently, these capacitors can be represented as a single state. The equivalent capacitor C_{eq} and its voltage $v_{C_{eq}}$ are defined as follows:

$$\begin{cases} C_{eq} = \dfrac{C_1 C_2}{C_1 + N^2 C_2} \\ v_{C_{eq}}(t) = N v_{C_1}(t) + v_{C_2}(t) \end{cases}. \tag{4}$$

This approach streamlines the analysis and controller design of the Cuk converter by consolidating the number of states considered.

The state-space representation for the Cuk-based SM is given by:

$$\dot{x}(t) = \sum_{i=1}^{2} \left(A_i x(t) + B_i u(t) \right), \tag{5}$$

where $x(t) = [i_{L_1}(t)\ v_{C_{eq}}(t)\ i_{L_2}(t)\ v_{C_o}(t)]^T$, $u(t) = [v_g(t)\ v_{in}(t)]^T$, and $y(t) = [i_o(t)]$ represent the state, input, and output vectors of the SM, respectively.

The matrices A_i, B_i, and C_i (where i represents ON or OFF states) correspond to the system, input, and output matrices, respectively.

Under the small-signal alternating current (AC) analysis, the line-to-control transfer function $G_d(s)$ is derived as:

$$G_d(s) = \frac{\tilde{v}_o(s)}{\tilde{d}(s)} = \frac{s^2 \left[\frac{RV_{in}C_1L_1}{1-D}\right] - s\left[\frac{D^2 V_{in} L_1}{(1-D)^2}\right] + RV_{in}}{\Delta}, \tag{6}$$

where $\Delta = s^4 [RC_1C_2L_1L_2] + s^3 [C_1L_1L_2] + s^2 \left[RC_2L_2(1-D)^2 + RC_2L_1D^2 + RC_1L_1\right] + s\left[L_2(1-D)^2 + L_1D^2\right] + R(1-D)^2$.

The RHP zeros in the Cuk converter's transfer function indicate non-minimum phase behaviour. This means that the system initially responds in the opposite direction to an input control signal before eventually correcting itself. This characteristic complicates system control, as RHP zeros introduce phase lag, reducing the available phase margin (PM). Consequently, the system becomes more susceptible to instability in feedback control scenarios.

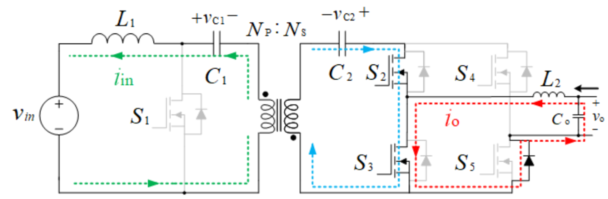

(a) ON-state (t_{ON})

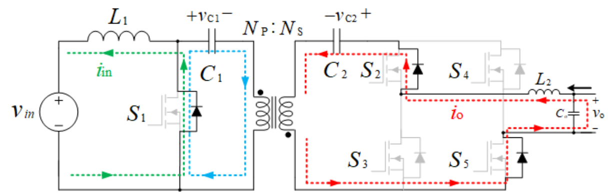

(b) OFF-state ($t_{\mathrm{OFF}} = t_s - t_{\mathrm{ON}}$)

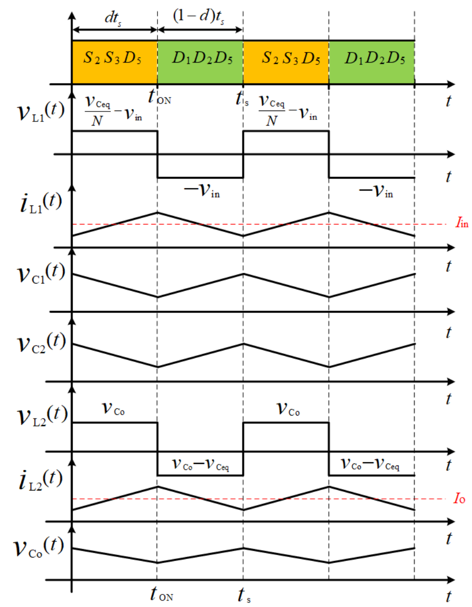

(c) Key waveforms for the positive half-cycle

Fig. 3 : Rectifier operation of the Cuk-based SM in the positive half-cycle $v_o > 0$

IV. Controller Design

To regulate the operation of the modular OBC topology, two distinct control systems are implemenInted:

1) Driving/Braking Mode Controller : This controller manages the stator voltages for the PMSM,

facilitating the desired velocity profile during both driving and regenerative braking modes.

2) Charging Mode Controller: This controller operates when the AC grid is connected to the outputs of the series-connected SMs for battery charging. It regulates the charging current, ensuring efficient and safe power transfer from the AC grid to the battery packs.

A. Driving Mode

Fig. 4 illustrates the control system for normal driving mode. The driver sets the desired linear speed V^* using the accelerator pedal, which is then converted to the rotational reference speed ω_m^*. This speed is regulated by a Proportional-Integral (PI) controller ($G_{\text{PI}}(s) = K_p + \frac{k_i}{s}$), which produces the reference electromagnetic torque T_e^* necessary to achieve the required mechanical torque T_m.

The inner loop PI controllers manage the d and q components of the PMSM's stator currents through the stator voltages v_a^*, v_b^*, and v_c^*. As shown in Fig. 1, each stator voltage is the aggregate of the voltages from the SMs in each phase. Since the same stator currents flow through all series-connected modules, the individual SM voltages can be adjusted to better balance the state-of-charge (SoC) across the battery packs as:

$$v_{okj}^* = \frac{v_j^*}{\sum_{i=i}^{m} V_{ini}} V_{ink}, \quad \text{where} \quad j = \{a, b, c\}. \tag{7}$$

Although torque control is typically used in EVs, speed control was selected in this paper due to its direct compatibility with the modular OBC topology, simplified driver input interpretation, and energy management considerations. As discussed above, the outer speed loop generates a torque reference, which is then regulated by inner current control loops, ensuring smooth operation.

B. Braking Mode

The modular OBC supports regenerative braking, which transfers kinetic energy back to the battery packs, thus conserving electrical energy and extending the EV's travel range. In regenerative braking mode, the reference torque T_m^* and consequently the q-axis component of the reference current I_q^* are negative. This necessitates each SM to function as an AC-to-DC rectifier to charge the battery packs, causing the battery currents $I_1 \ldots I_m$ to reverse direction.

During this charging process, the input voltages of the SMs are adjusted to ensure that battery packs with lower SoC receive a larger portion of the regenerated energy. Since the same current flows through all series-connected SMs within a phase, the individual voltages of the SMs are selected to balance the SoC across the battery packs as:

$$v_{okj}^* = \frac{v_j^*}{V_{ink} \sum_{i=i}^{m} \frac{1}{V_{ini}}}, \quad \text{where } j = \{a, b, c\}. \tag{8}$$

From (8), the magnitude of any battery pack's current will be inversely proportional to the battery pack's SoC to provide better balance and energy management.

C. Charging Mode

With the bidirectional power flow capability of the SMs, the three-phase currents i_{ga}, i_{gb}, and i_{gc} can flow from the grid to the battery packs. For a desired charging power P_{ch}^*, the peak reference current for both the grid and the Modular OBC is determined by $I_g^* = \frac{2P_{ch}^*}{3V_g}$.

Fig. 5 illustrates the controller during charging, where three proportional resonant (PR) controllers ($G_{\text{pr}}(s) = k_p + \frac{k_r \cdot s}{s^2 + \omega_0^2}$) regulate the three-phase currents from the grid. Consistent with the braking mode, the individual SM voltages are computed as described in equation (8). This approach ensures that the battery pack currents are inversely proportional to their SoCs, thereby maintaining the battery packs' voltage at its nominal value. Additionally, the sum of the individual SMs' voltages is adjusted to match the required phase voltages v_a, v_b, and v_c, ensuring that the charging operation achieves P_{ch}^* and operates at a unity power factor.

V. Genetic Algorithm (GA)

Designing PI and PR controllers for a Cuk converter with RHP zeros presents significant challenges. Employing a GA to optimise these controller gains offers several advantages, as it ensures a balance between stability, transient response, and steady-state error, adjusts the gains to mitigate the adverse effects of RHP zeros, and explores the design space more thoroughly than manual tuning methods, potentially leading to better outcomes.

In this study, a GA is applied to fine-tune the gains of the PR controllers used for grid current regulation during the charging mode. The goal is to optimise the proportional gain k_p and the resonant gain k_r to meet essential stability criteria for effective grid current control. The GA aids in achieving the desired gain margin (GM) and phase margin (PM), aligning with loop-shaping techniques aimed at shaping the loop transfer function to meet specific performance criteria.

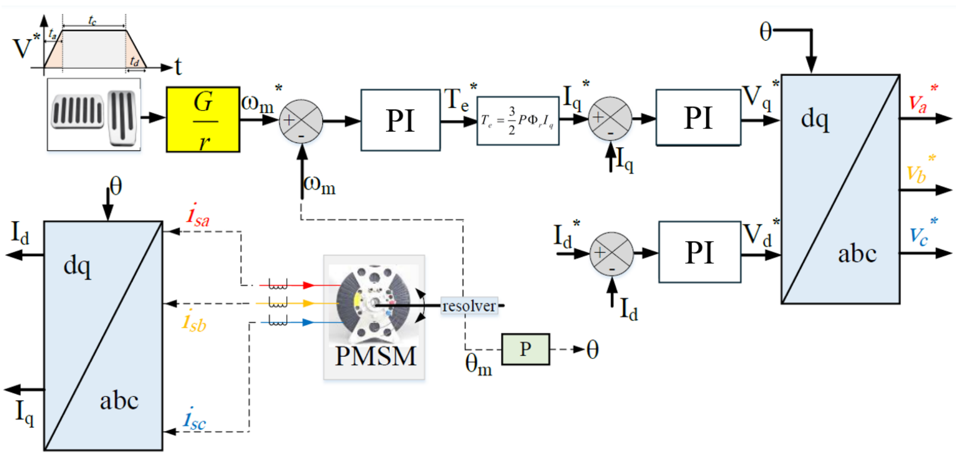

Fig. 4 : Driving and regenerative braking control system

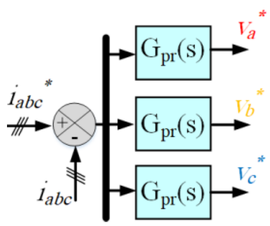

Fig. 5 : Block diagram of the charging mode controller

A. Problem Formulation for PR Controller optimisation

The goal is to design a PR controller that optimally controls grid current, achieving specific stability criteria: a GM of approximately 20 dB and a PM greater than 60°. To evaluate how well the controller meets these criteria, a fitness function is used in the GA, which is formulated as:

$$\begin{aligned} J(k_p, k_r) = w_1 \cdot |GM_{\text{desired}} - GM_{\text{actual}}| \\ + w_2 \cdot |PM_{\text{desired}} - PM_{\text{actual}}|, \end{aligned} \tag{9}$$

where $|GM_{\text{desired}} - GM_{\text{actual}}|$ and $|PM_{\text{desired}} - PM_{\text{actual}}|$ are the deviations of the actual GM and PM from the desired values, respectively. The weights w_1 and w_2 balance the importance of each criterion in the optimisation process.

B. GA optimisation Methodology

The GA optimisation methodology involves the following key steps:

1) **Initialisation**: Generate an initial population of candidate solutions, where each individual represents a potential pair of PR controller gains (k_p, k_r). Set system parameters, including resistance R, inductances L_1 and L_2, capacitances C_1 and C_2, input voltage V_{in}, and duty cycle D, to their respective values. Define bounds for k_p and k_r and initialise GA options such as population size and maximum number of generations.
2) **Evaluation**: Simulate the power system with the obtained PR controller gains. Compute the gain margin and phase margin for each solution using the system's transfer function. The fitness function evaluates how well each set of gains meets the desired stability criteria, specifically targeting a GM of approximately 20 dB and a PM greater than 60°.
3) **Selection**: Select individuals with the best fitness scores to act as parents for the next generation. The fittest individuals are more likely to contribute desirable traits to the next generation.
4) **Crossover**: Apply crossover operators to combine the gains k_p and k_r from selected parents. This process creates new offspring that inherit traits from both parents, exploring new configurations of PR controller gains.
5) **Mutation**: Introduce random changes to some offspring's gains to maintain genetic diversity. Mutation helps the algorithm avoid local optima and explore a broader solution space.
6) **Replacement**: Replace some or all of the old population with the new offspring. This ensures that the population evolves over time, progressively improving the solution.
7) **Termination**: Repeat the evaluation, selection, crossover, mutation, and replacement steps until a termination criterion is met, such as a maximum

number of generations or achieving a satisfactory fitness level.

The algorithm 1 summarises the PR controller optimisation process using the GA, where lb=lower band and ub=upper band.

Algorithm 1 Optimisation of PR Controller Gains Using GA

```
Input: System parameters R, L1, L2, C1, C2, Vin, D
Output: Optimised values for kp and kr
Initialise GA:
Define bounds for kp and kr as lb = [0, 0] and ub = [10, 10]
Set GA options: PopulationSize = 100, MaxGenerations = 50, Display = "iter"
Initialise population of candidate solutions
Define desired stability criteria:
Desired Gain Margin (GM) ← 20 dB
Desired Phase Margin (PM) ← 60°
while termination criteria are not met do
    Evaluate the fitness of each candidate:
    for each candidate in the population do
        Calculate system transfer function G(s) using the given parameters
        Define PR controller transfer function Gpr(s) with current kp and kr
        Compute GM and PM of the closed-loop system with Gpr(s)
        Compute deviations from desired criteria:
            Deviation of GM ← |GM_desired − GM_actual|
            Deviation of PM ← |PM_desired − PM_actual|
    end for
    Selection: Choose the fittest candidates based on their fitness scores
    Crossover: Generate new candidate solutions by combining traits of selected candidates
    Mutation: Introduce random changes to some candidates to maintain diversity
    Replace old population with new candidates
end while
Return Optimised gains kp and kr
```

VI. Verification

A. Simulations

In this study, a GA was employed to fine-tune the proportional gain (k_p) and resonant gain (k_r) of a PR controller designed for a Cuk converter system. The main goal was to meet specific stability criteria: a GM of approximately 20 dB and a PM greater than 60°.

The simulation involved defining the system's transfer function and using the GA to explore and optimise the controller gains. After running several GA iterations, the optimised gains were determined to be $k_p = 2.345$ and $k_r = 0.950$. These gains resulted in a GM close to the target of 20 dB and a PM exceeding 60°, as verified by the Bode plot and margin analysis of the closed-loop system, shown in Fig. 6a.

Fig. 6b presents a 3D scatter plot illustrating the relationship between k_p, k_r, and the fitness function J. Each point on the plot represents a set of k_p and k_r values and their corresponding fitness function J. The minimum value of J = 0.123 corresponds to the optimised gains, demonstrating the GA's effectiveness in identifying the optimal parameter set for the PR controller.

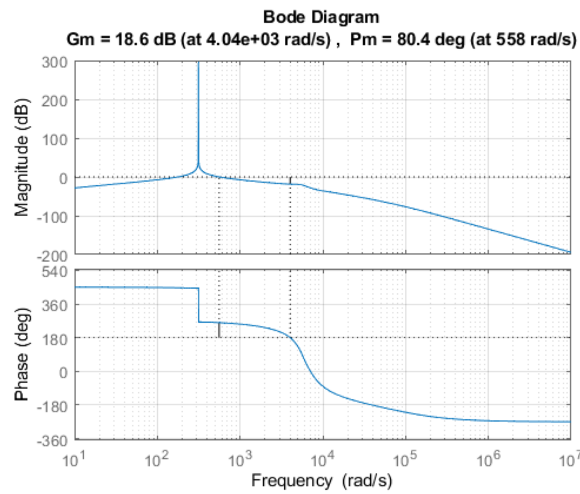

(a) Bode plot

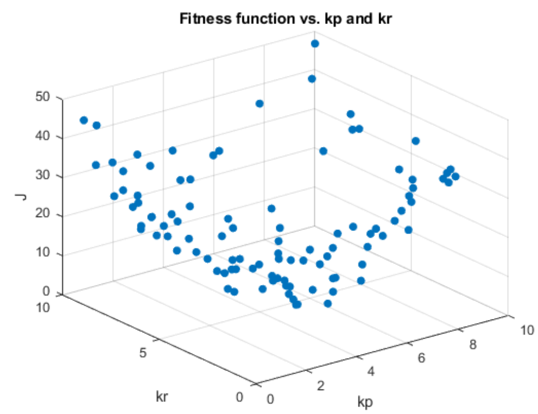

(b) Fitness function J versus k_p and k_r

Fig. 6 : Simulation results using GA

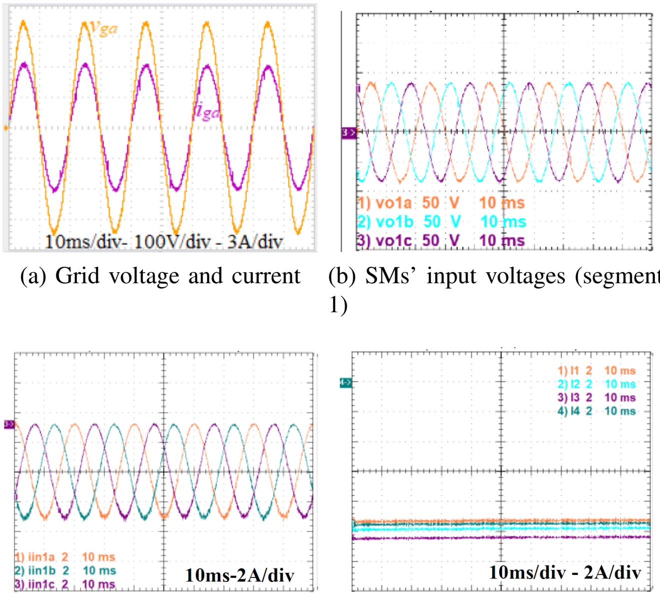

(a) Grid voltage and current

(b) SMs' input voltages (segment 1)

(c) SMs' output currents (segment 1)

(d) Battery segments' currents

Fig. 7 : Experimental results: charging mode

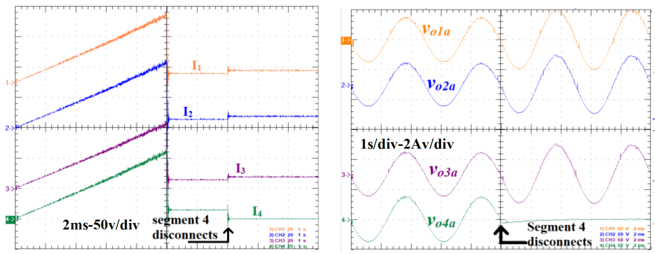

(a) battery segments' currents

(b) Individual voltages of SMs in phase "a"

Fig. 8 : Experimental results for charging mode under partial fault in battery segment 4

B. Experimental results

Experiments were carried out to evaluate the modular OBC's performance in charging mode under both normal and faulty conditions. During these tests, the switch SW_{abc} disconnected the modular OBC from the motor and connected its terminals to the AC grid. The charging power was limited to 3 kW, with each SM providing 250 W, and four SMs per phase were used. Since the power flow direction was from the grid to the batteries through the modular charger, the input and output definitions were reversed compared to other modes.

In Fig. 7a, the grid voltage at the point of common coupling (PCC) is shown along with the phase a current. Fig. 7b shows the individual input voltages for the first segment, specifically v_{ola}, v_{olb}, and v_{olc}. Fig. 7c illustrates the output current of the SMs in the first segment. Fig. 7d displays the currents through the battery segments, where negative currents indicate that the battery packs are being charged.

The DC voltages for the battery segments during the experiment were measured as: $V_{\text{in}_1} = 79.2\,\text{V}$, $V_{\text{in}_2} = 77\,\text{V}$, $V_{\text{in}_3} = 74.8\,\text{V}$, and $V_{\text{in}_4} = 78.32\,\text{V}$.

Fig. 8 illustrates the scenario where one battery segment (segment 4) was intentionally disconnected to simulate a partial fault condition. This test evaluated the system's ability to maintain stable operation and power distribution despite a segment failure. The fault was introduced during the charging process, and the system response was monitored to evaluate its robustness.

As shown in Fig. 8a, the battery segment currents before and after the fault event indicate a redistribution of current among the remaining segments. Upon disconnection of segment 4, the charging currents of the remaining segments (I_1, I_2, and I_3) increased proportionally to compensate for the missing segment, ensuring that the overall charging power remained constant at 3 kW. This self-balancing capability is a key advantage of the modular architecture and its control, as it allows the system to continue operating without requiring immediate intervention. Fig. 8b presents the individual voltages of the SMs in phase "a" before and after the fault occurrence. Despite segment 4's disconnection, the voltages of the remaining SMs remained stable, demonstrating the system's ability to regulate voltage effectively. The smooth transition in voltage levels indicates that the modular OBC successfully adjusted its control strategy to maintain continuous charging operation without introducing large voltage fluctuations or disruptions.

VII. Conclusion

This paper presents the operation and control of a modular OBC using single-stage Cuk-based converters as SMs. The Cuk inverter design, characterised by continuous input and output currents, combined with modularisation, enhances the reliability and adaptability of the modular charger for EV applications. RHP zeros are effectively managed through GA-based controllers, optimising performance across multiple operational modes, including driving, regenerative braking, and charging. Experimental results validate the system's robustness under both normal and partial fault conditions, demonstrating its ability to maintain stable operation and efficient power management. These findings highlight the modular OBC's potential for improving EV charging infrastructure, ensuring enhanced performance, scalability, and fault tolerance.

References

[1] Z. Hu, R. T. Mehrjardi, and M. Ehsani, "On the lifetime emissions of conventional, hybrid, plug-in hybrid, and electric vehicles," *IEEE Trans. Ind. Appl.*, vol. 60, no. 2, pp. 3502-3511, Mar.-Apr. 2024.

[2] Y. Feng, H. Zhu, and Z. Dong, "Simultaneous and global optimizations of LNG-fueled hybrid electric ship for substantial fuel cost, CO_2, and methane emission reduction," *IEEE Trans. Transp. Electrific.*, vol. 9, no. 2, pp. 2282-2295, Jun. 2023.

[3] F. N. Esfahani, A. Darwish, and A. Massoud, "PV/battery grid integration using a modular multilevel isolated SEPIC-based converter," *Energies*, vol. 15, no. 15, p. 5462, 2022.

[4] U. Fesli and M. B. Ozdemir, "Electric vehicles : A comprehensive review of technologies, integration, adoption, and optimization," *IEEE Access*, vol. 12, pp. 140908-140931, 2024.

[5] A. D. Badawy, S. Sfranciog, J. T. Hiranoyama, J. L. Ibarrola, J. Engstrom, K. Mikhail, and A. Dexter, "Low-voltage control circuits of Formula Student electric racing cars," *Hardware*, vol. 2, no. 3, pp. 190-222, 2024.

[6] O. Bay, M. T. Tran, M. El Baghdadi, S. Chakraborty, and O. Hegazy, "A comprehensive review of GaN-based bidirectional on-board charger topologies and modulation methods," *Energies*, vol. 16, no. 12, p. 3433, 2023.

[7] S. A. Q. Mohammed and J. -W. Jung, "A comprehensive state-of-the-art review of wired/wireless charging technologies for battery electric vehicles : Classification, common topologies, future research issues," *IEEE Access*, vol. 9, pp. 19572-19585, 2021.

[8] J. Wyss and J. Biela, "Optimized bidirectional PFC rectifiers and inverters—Si vs. SiC vs. GaN in 2L and 3L topologies," in *Proc. IEEE Int. Power Electron. Conf. (IPEC-ECCE Asia)*, Niigata, Japan, pp. 3734-3741, 2018.

[9] F. N. Esfahani, A. Darwish, X. Ma, and P. Twigg, "Non-integrated and integrated on-board battery chargers (iOBCs) for electric vehicles (EVs) : A critical review," *Energies*, vol. 17, no. 10, p. 2285, 2024.

[10] J. Cai and X. Zhao, "An on-board charger integrated power converter for EV switched reluctance motor drives," *IEEE Trans. Ind. Electron.*, vol. 68, no. 5, pp. 3683-3692, May 2021.

[11] H. Cheng, L. Wang, L. Xu, X. Ge, and S. Yang, "An integrated electrified powertrain topology with SRG and SRM for plug-in hybrid electrical vehicle," *IEEE Trans. Ind. Electron.*, vol. 67, no. 10, pp. 8231-8241, Oct. 2020.

[12] F. N. Esfahani, A. Darwish, and X. Ma, "Design and control of a modular integrated on-board battery charger for EV applications with cell balancing," *Batteries*, vol. 10, no. 1, p. 17, 2024.

[13] J. Lu, H. Zhao, Y. Fan, Y. Kang, Z. Liu, and Z. Chen, "A modular-designed three-phase high-efficiency high-power-density EV battery charger using dual/triple-phase-shift control," *IEEE Trans. Power Electron.*, vol. 33, no. 9, pp. 8091-8100, Sep. 2018.

[14] F. N. Esfahani, A. Darwish, S. Alotaibi, and F. Campean, "Hierarchical control design of a modular integrated OBC for dual-motor electric vehicle applications," *IEEE Access*, 2024.

[15] S. E. Schulz, "Exploring the high-power inverter : Reviewing critical design elements for electric vehicle applications," *IEEE Electrification Mag.*, vol. 5, no. 1, pp. 28-35, Mar. 2017.

[16] A. Khaligh and M. D'Antonio, "Global trends in high-power on-board chargers for electric vehicles," *IEEE Trans. Veh. Technol.*, vol. 68, no. 4, pp. 3306-3324, Apr. 2019.

[17] A. Sewergin, A. H. Wienhausen, and K. Oberdieck, "Modular bidirectional full-SiC DC-DC converter for automotive application," in *Proc. IEEE Int. Conf. Power Electron. Drive Syst. (PEDS)*, Honolulu, HI, USA, pp. 277-281, 2017.

[18] S. Taraborrelli, R. Spenke, and R. W. D. Doncker, "Bidirectional dual active bridge converter using a tap changer for extended voltage ranges," in *Proc. Eur. Conf. Power Electron. Appl. (EPE ECCE Europe)*, pp. 1-10, 2016.

[19] G. Yang, E. Draugedalen, T. Sorsdahl, H. Liu, and R. Lindseth, "Design of high efficiency high power density 10.5kW three-phase on board charger for electric/hybrid vehicles," in *Proc. PCIM Europe 2016*, Nuremberg, Germany, pp. 1-7, 2016.

[20] P. M. Johnson and K. H. Bai, "A dual-DSP controlled SiC MOSFET based 96%-efficiency 20kW EV on-board battery charger using LLC resonance technology," in *Proc. IEEE Symp. Ser. Comput. Intell.*, Honolulu, HI, USA, pp. 1-5, 2017.

[21] F. N. Esfahani and A. Darwish, "Regenerative braking for EVs using PMSM with CHB as bidirectional traction converter," in *Proc. IEEE Int. Conf. Compatibility, Power Electron., Power Eng. (CPE-POWERENG)*, Birmingham, UK, Jun. 2022, pp. 1-7.

[22] F. N. Esfahani, J. Ebrahimi, A. Bakhshai, X. Ma, and A. Darwish, "Regenerative braking for EVs using a brushless DC motor and multi-level bidirectional traction converter," in *Proc. IEEE Can. Conf. Electr. Comput. Eng. (CCECE)*, Kingston, ON, Canada, 2024, pp. 223-227.

[23] S.-E. Ong and K. Coffey, "Understanding the impact of IEC 60747-17 on capacitive and magnetic couplers," in *Proc. PCIM Eur.*, Nuremberg, Germany, 2024, pp. 2937-2942.